Heliyon 9 (2023) e20329

Contents lists available at ScienceDirect

Heliyon

journal homepage: www.cell.com/heliyon

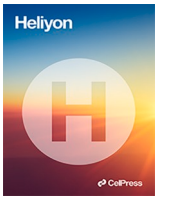

Integrative metabolome and lipidome analyses of plasma in neovascular macular degeneration

Tantai Zhao [a,b], Jiani Li [a,b], Yanbin Wang [a,b], Xiaojian Guo [a,b], Yun Sun [a,b,*]

[a] Department of Ophthalmology, the Second Xiangya Hospital, Central South University, Changsha, Hunan, China
[b] Hunan Clinical Research Center of Ophthalmic Disease, Changsha, Hunan, China

ARTICLE INFO

Keywords:
Age-related macular degeneration
Glycerophospholipid pathway
Lipidomics
Metabolomics
Sphingolipid pathway

ABSTRACT

Age-related macular degeneration (AMD) causes irreversible vision-loss among the elderly in industrial countries. Neovascular AMD (nAMD), which refers to late-stage AMD, is characterized by severe vision-threatening choroidal neovascularization (CNV). Herein, we constructed a global metabolic network of nAMD, based on untargeted metabolomic and lipidomic analysis of plasma samples collected from sixty subjects (30 nAMD patients and 30 age-matched controls). Among the nAMD and control groups, 62 and 44 significantly different metabolites were detected in the positive and negative ion modes, respectively. Grouping analysis further showed that lipid and lipid-like molecule-based superclasses contained the highest number of significantly different metabolites. Lipidomic analysis revealed that 53 lipids among the nAMD and control groups differed significantly; these belonged to four major lipid categories (glycerophospholipids, sphingolipids, glycerolipids, and fatty acids). A discriminative biomarker panel comprising 16 metabolites and lipids, which was constructed using multivariate statistical machine learning methods, could effectively identify nAMD cases. Among these 16 compounds, eight were lipids that belonged to three lipid categories (glycerophospholipids, sphingolipids, and prenol lipids). The top three biomarkers with the highest importance scores were all lipids (a glycerophospholipid and two sphingolipids), highlighting the crucial role played by glycerophospholipid and sphingolipid pathways in nAMD. These differences between the metabolic and lipid profiles of nAMD patients and elderly individuals without AMD provide a readout of the overall metabolic status of nAMD. Further insights into the identified discriminative biomarkers may pave the way for future diagnostic and therapeutic interventions for nAMD.

1. Introduction

Age-related macular degeneration (AMD) is the leading cause of irreversible vision loss in elderly people in industrialized countries [1]. AMD can be classified into two types: early AMD, which is characterized by drusen or pigmentary abnormalities, and late AMD, which can be further classified into neovascular AMD (nAMD, or "wet" AMD) and geographic atrophy (GA) [2]. Intravitreal injection of anti-vascular endothelial growth factor (VEGF) agents is the recommended first treatment approach for nAMD, which is characterized by choroidal neovascularization (CNV) and results in a cascade of sight-threatening complications such as retinal hemorrhage,

* Corresponding author. Department of Ophthalmology, the Second Xiangya Hospital, Central South University, and Hunan Clinical Research Center of Ophthalmic Disease, 139 Middle Renmin Road, Changsha, Hunan, 410011, China.
E-mail address: suny58@csu.edu.cn (Y. Sun).

https://doi.org/10.1016/j.heliyon.2023.e20329
Received 31 May 2023; Received in revised form 9 September 2023; Accepted 19 September 2023
Available online 21 September 2023

retinal pigment epithelial (RPE) detachment, hard exudates, and subretinal fibrous scar tissue formation [2].

Age is the main risk factor that consistently contributes to AMD development [2,3]. In addition, oxidative stress caused by compromised retinal antioxidative defense systems associated with aging, is also known to contribute to AMD pathogenesis [4]. Noteworthy, not all elderly individuals develop AMD; indeed, AMD prevalence among elderly Asian and white populations is estimated to be only 6.8% and 8.8%, respectively [5]. In contrast, the global prevalence of age-related cataract, which is an ophthalmological condition triggered by the same risk factors of AMD, is estimated to be 17.2% [6].

The human retina is a metabolically active tissue that comprises products and intermediates of metabolism, as well as downstream products of the cumulative effects of certain pathological conditions [7,8]. Therefore, in recent years, the metabolomic profile of AMD has attracted significant attention from researchers. Previous studies, which used nuclear magnetic resonance (NMR) spectroscopy- or mass spectrometry (MS)-based metabolomics approaches, identified several differential metabolites in the plasma of nAMD patients compared with those of controls [9–11], which demonstrated that altered metabolite profiles may reveal clues on the dysfunctional or perturbed metabolic pathways that underlie AMD pathogenesis. Previous studies also explored the plasma metabolomic profile of AMD at different severity stages [12,13]. Evaluation of two large independent cohorts of AMD patients using NMR spectroscopy-based metabolomics revealed small changes in the levels of some amino acids, organic acids, creatine, dimethyl sulfone, as well as for some fatty acids and cholesterol-related molecules [12]. Furthermore, MS-based metabolomics identified 28 metabolites, differing significantly between the patients and controls, and 67 metabolites differing with the stage of the disease [13]. In addition, 87 discriminant metabolites in the plasma were identified to be associated with early, intermediate, and late-stage AMD, most of which belonged to lipid pathways, and in particular, the glycerophospholipid pathway [14]. Although previous studies have highlighted the dysregulation of lipid metabolic pathways in AMD [13,15], these investigations only used metabolomic (and not lipidomic) approaches; therefore, they only provide a partial perspective on the role of lipids in AMD.

The present study aimed to close this knowledge gap by exploring the plasma metabolomic and lipidomic signatures of nAMD patients *vs.* controls, and by constructing a global metabolic network of nAMD. For this purpose, age-matched nAMD and non-AMD individuals were subjected to untargeted metabolomic and lipidomic analyses designed to identify any plasma metabolites, lipids, and/or their derivatives that had been altered. To further elaborate on the circulating "global metabolome" and to detect the most discriminative biomarkers of nAMD, integrated global metabolomic and lipidomic approaches were applied using multivariate statistical machine learning methods. Taken together, the findings of this study are expected to provide new foundations for future diagnosis and therapeutic intervention tools for nAMD.

2. Material and methods

2.1. Subjects and plasma sample collection

Sixty Chinese subjects (30 nAMD patients and 30 age-matched controls) were enrolled in the study. For each subject, the diagnosis, demographic data, medical history, preoperative fundus examination results, biochemical parameters, and date of sample collection were recorded. Informed consent was obtained from all patients prior to enrolment, and consent was obtained from all patients for publication of the data and images presented in the article. The study was conducted according to the tenets of the Declaration of Helsinki and with the approval of the institutional review board from the Second Xiangya Hospital of Central South University (No. 2020-094). The nAMD group met the following inclusion criteria: absence of any ocular diseases other than nAMD (*i.e.*, ocular infectious disease, diabetic retinopathy, retinal vein occlusion, glaucoma, uveitis, ocular trauma); refractive error between +6.0 and −6.0 diopters spherical equivalent. Intravitreal injection of anti-VEGF agents was a requirement for enrollment in the study for all patients with nAMD. The CNV in the AMD patients enrolled in our study was classified as type 1 if it originated from the choriocapillaris and was localized under the RPE, or as type 2 neovascularization if it originated from the choriocapillaris but proliferated above the RPE in the subretinal space, according to the Consensus on Neovascular AMD Nomenclature Study Group (CONAN) [2,16,17]. Patients with type 3 neovascularization (or retinal angiomatous proliferation) were excluded from the study. The age-matched control group met the following inclusion criteria: diagnosis of age-related cataracts but with absence of other ocular diseases (including AMD). History of prior cataract or retinal surgery, or any other treatment (including pan-retinal photocoagulation or intravitreal injection) within three months before study start was considered as exclusion criterion. Patients with diabetes, thyroid disease, or any other metabolic diseases that could influence the systemic metabolic status were also excluded. Participants were thoroughly evaluated using fundus examinations, including ultra-widefield fundus photography (Optos Daytona Ultra-Widefield Fundus System, Optos, Dunfermline, Scotland, United Kingdom), fluorescein angiography (Spectralis HRA-OCT, Heidelberg Engineering, Heidelberg, Germany), spectral domain optical coherence tomography (Spectralis, Heidelberg, Germany, or Optovue, Fremont, California, CA, USA) examinations, and slit lamp ophthalmoscopy with a 90-diopter lens. Three experienced ophthalmologists (T Zhao, X Guo, and Y Sun), who were blinded to the clinical data of the participants, provided the diagnosis based on examination results.

Standardized methods were used to obtain venous blood samples from fasting patients at the Department of Ophthalmology, Second Xiangya Hospital of Central South University, Hunan, China. Fasting blood samples were placed in 5 mL vacutainer tubes containing ethylenediamine tetra-acetic acid, and centrifuged (1500×*g*, 4 °C) for 15 min. Each aliquot (500 μL) of plasma was immediately cooled and stored at −80 °C until further analysis.

2.2. Chemicals and reagents

Ammonium acetate, and high-performance liquid chromatography (HPLC)-grade formic acid and ammonium formate were

purchased from Sigma-Aldrich (St. Louis, MO, USA). Ammonium hydroxide, MS-grade methanol and acetonitrile, and HPLC-grade 2-propanol were purchased from Thermo Fisher Scientific (Waltham, MA, USA).

2.3. Sample preparation and metabolites/lipids extraction

Stored plasma samples were thawed at 4 °C. To remove their protein content, 100 μL aliquots were mixed with 400 μL of cold methanol/acetonitrile (1:1, v/v), and centrifugated (14000×*g*, 4 °C) for 15 min. The supernatant was dried using a vacuum centrifuge. For liquid chromatography (LC)-MS analysis, the samples were re-dissolved in 100 μL of acetonitrile/water (1:1, v/v) solution. The lipid content was extracted according to the methyl-*tert*-butyl ether (MTBE) method [18]. Two internal standards, namely phenylalanine-carboxy-1-13C and glutamic-2,3,3,4,4-d5 acid, were used to validate the stability and repeatability of the analysis instrument. Moreover, quality control (QC) samples were prepared by pooling 10 μL of each sample and run at the beginning of the sample queue for column conditioning, as well as between samples every 10 injections. Blank samples without any biological material were run at the beginning of the sample queue for column conditioning, as well as between samples every 10 injections to avoid any interference, background noise, or contamination that may occur during the sample preparation, extraction, or analysis process.

2.4. Ultra-HPLC-quadrupole/time-of-flight MS/MS analysis for metabolomics

Analyses were performed using UHPLC (1290 Infinity LC system, Agilent Technologies, Santa Clara, CA, USA) coupled to a quadrupole time-of-flight mass spectrometer (AB Sciex Triple TOF 6600, Framingham, MA, USA). In brief, for hydrophilic interaction liquid chromatography (HILIC) separation, the samples were analyzed in both positive and negative modes using a 2.1 mm × 100 mm ACQUITY UPLC BEH 1.7 μm column (Waters Corporation, Milford, MA, USA) at a constant temperature of 25 °C. Mobile phase and gradient elution were performed as previously described [19,20]. The gradients were set at a flow rate of 0.5 mL/min, and a 2 μL aliquot of each plasma sample was injected. For quadrupole/time-of-flight (Q-TOF)-MS/MS analysis, electrospray ionization (ESI) source conditions were set as previously described [21]. For MS/MS tandem acquisition, the instrument was set as previously described [22], with the parameters set as follows: declustering potential = 60 V (+) and −60 V (−); and collision energy fixed at 35 ± 15 eV. MS/MS data were acquired using data-dependent acquisition (DDA) in high sensitivity mode , with the following settings: isotopes within 4 Da were excluded and candidate ions to monitor per cycle = 10. Continuous analysis of the samples was performed in a random sequence to avoid instrument detection signal fluctuations. QC samples were inserted into the analysis sequence to determine and evaluate the stability of the system and experimental data quality.

2.5. LC-MS/MS analysis for lipidomics

Analyses were performed using a UHPLC Nexera LC-30A system (SHIMADZU, Kyoto, Japan) coupled to a Q-Exactive system (Thermo Fisher Scientific) as previously described [23]. Briefly, lipid extracts were re-dissolved in 200 μL of 90% isopropanol/acetonitrile and centrifuged (14000×*g* for 15 min), after which a 2 μL sample was injected. Reverse phase chromatography was selected for LC separation using a CSH C18 column (1.7 μm, 2.1 mm × 100 mm; Waters Corporation) at a temperature of 45 °C. The mobile phase was set, gradient elution was performed as previously described [23], and a 2 μL aliquot of each plasma sample was injected. Mass spectra were acquired using Q-Exactive in both positive and negative ESI modes, for which the parameters were optimized and preset for all measurements as follows: heater temperature = 300 °C; capillary temperature = 350 °C; sheath gas flow rate = 45 arb; auxiliary gas flow rate = 15 arb; sweep gas flow rate = 1 arb; ion spray voltage = 3000 V; S-Lens RF Level = 50%; and scan range of the instruments: 200–1800 *m/z*. The mass-to-charge ratios (*m/z*) of the lipid molecules and fragments were recorded as previously described [24].

2.6. Data processing

Raw UHPLC-Q-TOF-MS/MS data were converted to MzXML files using ProteoWizard MSConvert [25] and subsequently imported into XCMS online software (https://xcmsonline.scripps.edu) for peak alignment, retention time correction, and peak area extraction. The following setting were used: centwave settings for feature detection $\Delta m/z = 10$ ppm, peakwidth = c (10, 60); obiwarp settings for retention time correction profStep = 1; and minfrac = 0.5, bw = 5 and mzwid = 0.025 for chromatogram alignment. After peak picking and grouping, the R "*CAMERA*" (Collection of Algorithms of MEtabolite pRofile Annotation) package, was used for the annotation of isotopes and adducts [26]. Identification of the metabolites was performed by comparing the accuracy of the *m/z* value (<10 ppm) and MS/MS spectra with that contained in the self-built commercial database established using available authentic standards (Shanghai Applied Protein Technology Co., Shanghai, China) [27–30]. After sum normalization, the processed data were analyzed using the SIMPCA-P 16.1 (Umetrics, Umea, Sweden) for multivariate analysis, including Pareto-scaled principal component analysis (PCA), partial least squares discriminant analysis (PLS-DA), and orthogonal partial least-squares discriminant analysis (OPLS-DA). Seven-fold cross-validation and response permutation testing procedures were performed to evaluate the robustness of the model. Variable importance in the projection (VIP) value from OPLS-DA modeling was used to identify the overall contribution of each variable. A Student's *t*-test was used to determine the significance of differences between two groups of independent samples. OPLS-DA VIP >1 and $p < 0.05$ were used to screen significantly changed metabolites [31]. Pearson's correlation analysis was performed to determine correlations between the two variables. The Human Metabolome Database (HMDB) (http://hmdb.ca/) was used to define the classes of metabolites, and ClassyFire (http://classyfire.wishartlab.com/), a web-based application for automated structural classification of

chemical entities [32], was used to compute the hierarchical chemical classification of the detected metabolites.

Lipid species were identified after the data was processed using LipidSearch software version 4.2 (Thermo Fisher Scientific) for peak alignment, retention time correction and peak area extraction. LipidSearch is a search engine used to identify lipid species based on MS/MS, and contains data on more than 30 lipid classes, with information on more than 1,500,000 ion fragments in its database [23]. Precursor and product tolerances were both set to 5 ppm, while the product ion threshold was set at 5%. For data extracted from LipidSearch, ion peaks with a value $>$ 50% missing were removed from the analysis. Following normalization and integration using the Pareto scaling method, the processed data were imported into SIMPCA-P 16.1 for multivariate statistical analysis, including PCA, PLS-DA, and OPLS-DA. Lipids showing significant differences were identified based on a combination of statistically significant thresholds of VIP $>$1 values obtained from the OPLS-DA model and a two-tailed Student's *t*-test ($p < 0.05$) performed on raw data.

2.7. Bioinformatic analysis

For Kyoto Encyclopedia of Genes and Genomes (KEGG) pathway annotation purposes, differentially expressed metabolites were annotated using the online KEGG database (https://www.genome.jp/kegg/) and mapped to KEGG pathways. To further explore the impact of differentially expressed metabolites, enrichment analysis was performed. KEGG pathway enrichment analyses were performed using the Fisher's exact test, considering the whole metabolites of each pathway as the background dataset. Only pathways with $p < 0.05$ were considered significant. Metabolite data were further analyzed by hierarchical clustering using the Euclidean distance algorithm as a similarity metric with an average linkage clustering algorithm from Cluster 3.0 (http://bonsai.hgc.jp/~mdehoon/software/cluster/software.htm) and Java Treeview (http://jtreeview.sourceforge.net). Heatmaps were generated using Pearson's correlation analysis to determine correlation between all variables. The resulting correlation networks and chord diagrams were visualized using Cytoscape version 3.8.2 (https://cytoscape.org) and R version 3.5 (R Foundation for Statistical Computing, Vienna, Austria).

2.8. Machine learning and screening of nAMD biomarkers

Prior to biomarker selection, the missing values were filled using K-nearest neighbor (KNN) imputation, and abundance was subjected to log10 transformation. The ensemble machine learning method was combined with multiple feature selection approaches and 10-fold cross-validation to identify potential robust biomarkers. Applying a voting procedure, we selected potential biomarkers with reward features appearing in the optimal subsets generated by the ensemble method. The selected features were ranked lower by their contribution to the classification model. Receiver operating characteristic (ROC) curve analysis was used to evaluate the potential predictive performance of the detected metabolites for distinguishing nAMD from controls [33,34]. The area under the ROC curve (AUC) represents the predictive performance of the metabolites distinguished between the groups [35]. Several highly ranked features that led to the highest and most stable AUC values of the model were considered as potential biomarkers. Diagnostic panel models of biomarkers were constructed using logistic regression (LR), random forest (RF) and support vector machine (SVM) methods. The maximum potential effectiveness of a biomarker was calculated using the Youden index to define the best cutoff value for diagnostic decision making [36]. To further evaluate the predictive performance of the diagnostic panel of biomarkers, the dataset was divided again into training and test sets at a ratio of 7:3, following which a repeated 10-fold cross-validation approach was used [37]. All algorithms were implemented using R version 3.5.

2.9. Statistical analyses

Statistical analyses were performed using SPSS 23.0 for Windows (IBM Corp., Armonk, NY, USA) and R version 3.5 unless noted otherwise. SIMPCA-P 16.1 (Umetrics, Umea, Sweden) was used for multivariate data analysis, including PCA, PLS-DA, and OPLS-DA. Results are presented as the mean $\pm$ standard deviation (SD). Student's *t*-tests, Pearson's correlation analysis, Pearson Chi-Square tests, Mann-Whitney U tests, and Fisher's exact tests were used, where appropriate. Statistical significance was set at $p < 0.05$.

3. Results

3.1. Study population

Sixty Chinese subjects (30 nAMD patients and 30 age-matched controls) were enrolled in the study. There was no age difference between two groups (65.30 $\pm$ 7.562 years old in nAMD group and 67.33 $\pm$ 6.408 years old in the control group, p = 0.180 by Mann-Whitney *U* test). The groups were similar concerning the smoking history and dietary patterns (similar consumption of fruits, vegetables, grains, fish, and red meat), and no gender-based differences were detected. The baseline demographic data in nAMD and control groups are summarized in Table S1. The information of visual acuity and fundus characteristics at baseline are summarized in Table S2, and representative baseline multimodal imaging from nAMD patients and controls are depicted in Fig. S1.

3.2. Metabolome profile of nAMD

A total of 18069 metabolites (9350 in positive ion mode and 8719 in negative ion mode) were detected, and 1254 were identified (719 in positive ion mode and 535 in the negative ion mode) in the in-house database of Shanghai Applied Protein Technology. Scores

plot, 7-fold cross-validation and response permutation tests from PLS-DA and OPLS-DA showed satisfactory discrimination between the nAMD and control groups (Fig. 1 & S2). Moreover, a clear separation between the nAMD and the control groups was observed based on the PLS-DA score plot in the positive (R2Y = 0.99, Q2 = 0.781) and negative (R2Y = 0.984, Q2 = 0.586) modes, indicating that nAMD had altered metabolites. The goodness-of-fit and predictive ability of the identified metabolites determined by the R2Y and Q2 values, respectively, suggested that they were all robust, with high reliability and predictive power [38].

Further grouping analysis revealed that the identified metabolites were related to 12 superclasses (Fig. 2A). In the positive mode, 62 metabolites showed significant differences between the nAMD and control groups, which were derived from 24 subclasses and six super-classes (Table S3). In the negative mode, 44 metabolites were significantly differentially expressed between the nAMD and control samples, which were derived from 22 subclasses and six superclasses (Table S4). Interestingly, lipids and lipid-like molecule superclasses showed the highest numbers of significantly differentially expressed metabolites (17/62 and 19/44 in positive ion and negative ion modes, respectively). Sulfadoxin, lactose, zolpidem, prostaglandin (PG) D2, 3-hydroxybenzyl alcohol, and D-(+)-melibiose contents were 3-fold higher in nAMD samples than controls. To be noted, despite sulfadoxin exhibited the highest magnitude of increase concerning its amount, it is deemed a suspicious false-positive due to its synthetic nature as an antibacterial and antimalarial agent.

Volcano maps of differential metabolites are shown (Fig. 2B) and superclass grouping was further visualized (Fig. 2C). The overall profile of the significantly altered metabolites in the plasma of nAMD patients *vs.* controls are illustrated in Figs. S3 and S4.

Next, the specific metabolic patterns of nAMD were further evaluated based on the differentially expressed metabolites using OPLS-DA for clustering, correlation, and pathway investigations. The VIP calculated using the PLS-DA and OPLS-DA models revealed the metabolites that contributed most to the difference between the nAMD and control groups. Differential metabolites in all enrolled

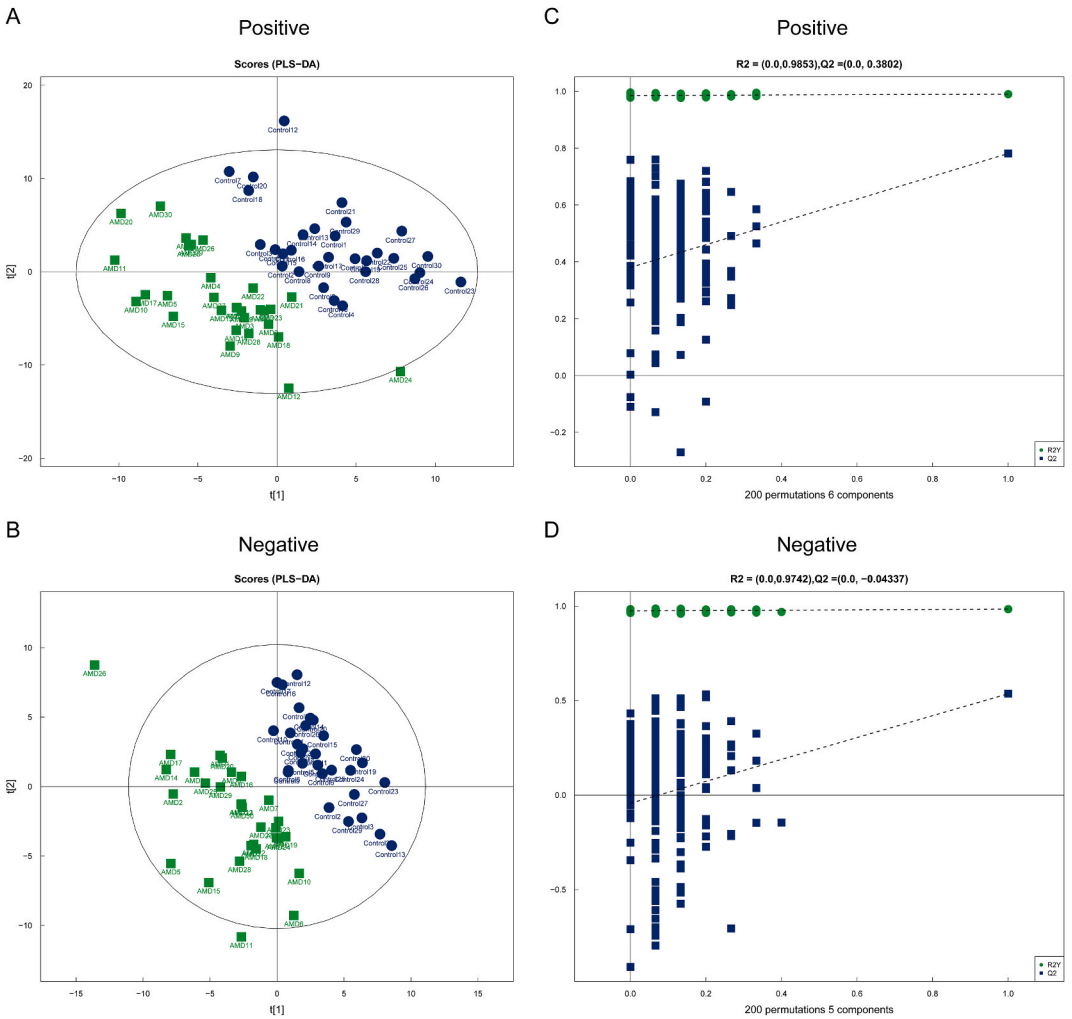

Fig. 1. Partial least square discriminant analysis (PLS-DA) of the neovascular age-related macular degeneration (nAMD) and control groups. A and B: Score plots of PLS-DA. C and D: 7-fold cross-validation and response permutation tests from PLS-DA. Upper figures and bottom figures were obtained in positive and negative ion mode, respectively.

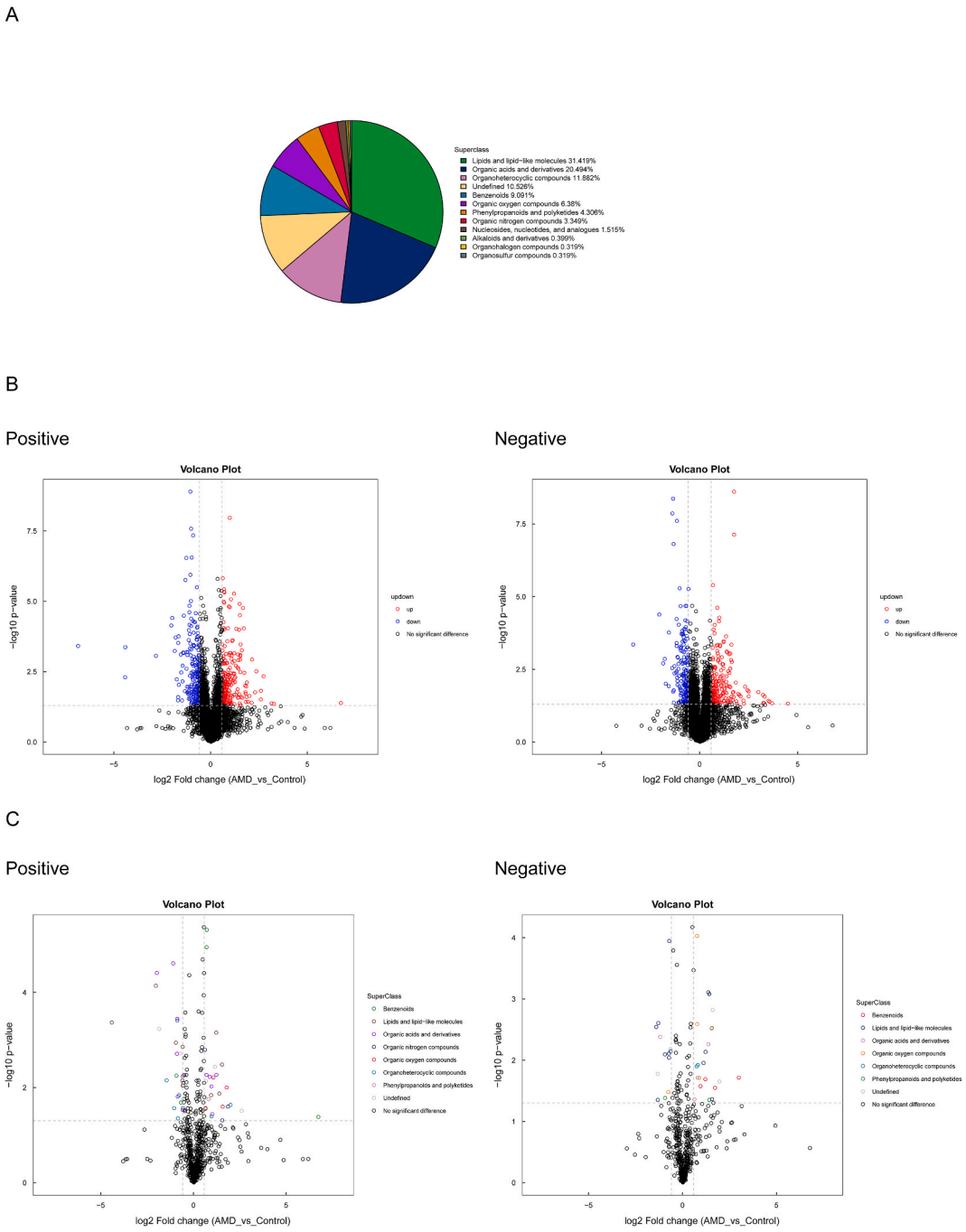

Fig. 2. Visualization of the overall profile of detected plasma metabolites in nAMD *vs.* control groups. A: Percentages of metabolites identified in their superclass according to their chemical taxonomy. B: Volcano map showing the overall profile of the detected plasma metabolites in the samples. Upregulated and downregulated metabolites are indicated by red and blue colors, respectively. C: Volcano map showing the superclass profile of detected plasma metabolites. The different metabolite superclasses are shown with distinct colors.

samples were visualized using a heatmap generated via hierarchical clustering analysis, which was based on the degree of similarity between metabolite abundance profiles [38] (Fig. 3A). Metabolic proximities between significantly different metabolites were determined via correlation analysis, being the metabolites either synergistically interconnected or mutually exclusive (Fig. 3B). A chord diagram was also designed for a more comprehensive understanding of the possible regulatory relationships between the metabolites (Fig. 3C).

Pathway analysis facilitates an understanding of the complex relationships between genes, proteins, and metabolites [38–40].

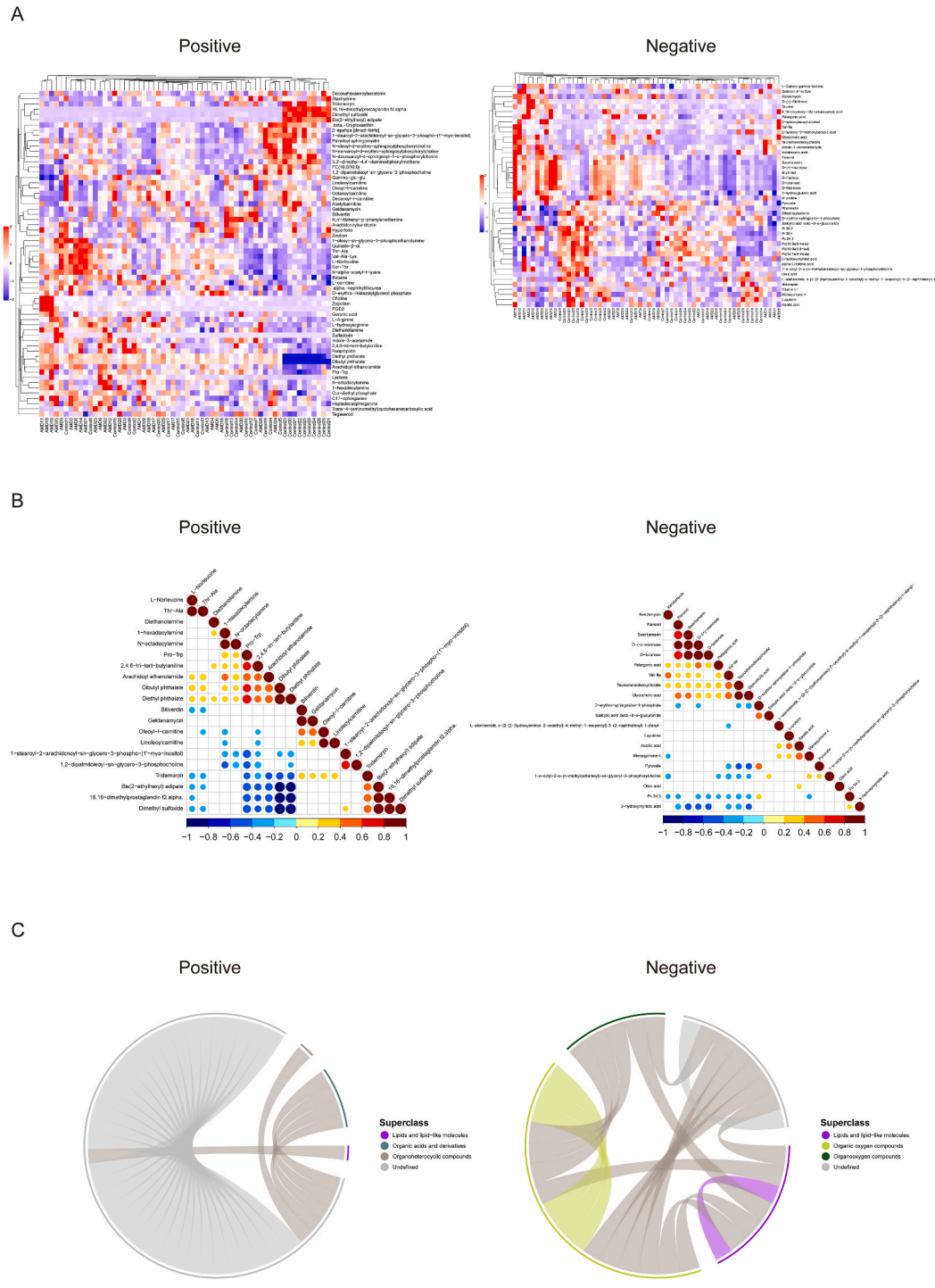

Fig. 3. Comparison between the differential expression of metabolites in nAMD and control groups. A: Heat map of the global metabolite profile in all plasma samples obtained via hierarchical clustering analysis. B: Correlation analysis of the metabolites showing significant differences between positive and negative polarity modes. Red and blue colors indicate positive and negative correlations, respectively, while the white color indicates non-significant correlation. Color intensity and circle sizes are proportional to the correlation coefficient (r value). C: Network visualization of the correlated metabolite pairs ($r > 0.8$ by Pearson's correlation analysis and $p < 0.05$ by Student's *t*-test) in positive and negative polarity modes. Each metabolite is represented by a node around the circle plot and color coded according to its superclass. Lines connecting highly correlated pairs are color coded according to metabolite superclass for intra-class correlation and are depicted in dark-grey for inter-class correlation.

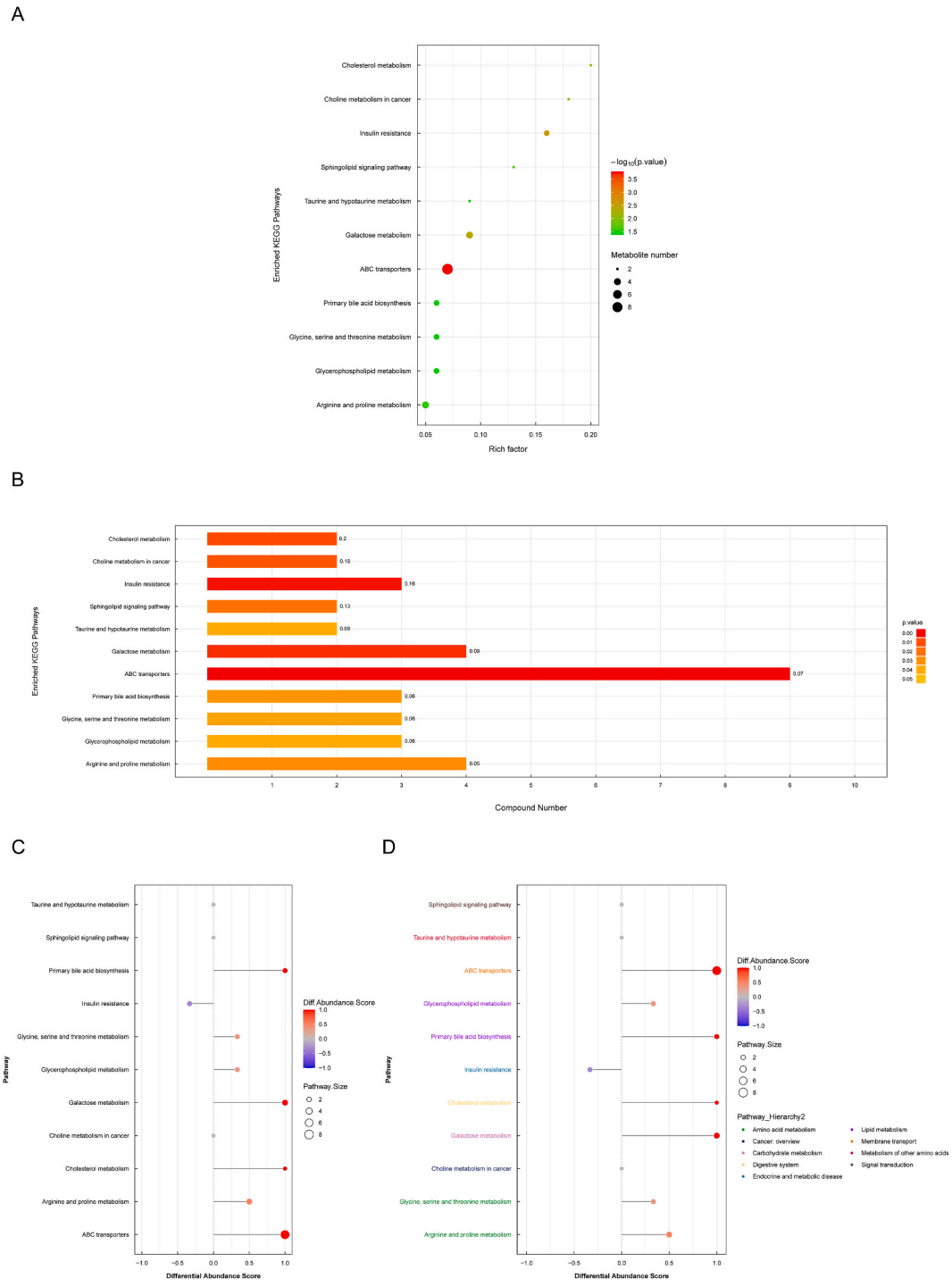

Fig. 4. KEGG pathway analysis of the significantly different metabolites between the nAMD and control groups. A: Bubble diagram depicting KEGG enriched pathways. B: Bar chart depicting KEGG enriched pathways; the number on the right side of each bar indicates the rich factors (number of different metabolites enriched in the pathway/number of all identified metabolites in the metabolites set). C: Pathway-based analysis of metabolic changes between groups. The differential abundance score captures the average of gross changes for all metabolites in a pathway. A score of 1 or −1 indicates that all measured metabolites in the pathway increased or decreased, respectively. D: Differential abundance scores in significantly enriched metabolites according to their pathway hierarchy.

Herein, KEGG enrichment analysis revealed 11 significantly different metabolic pathways between nAMD patients and controls (Fig. 4A; 4B), including cholesterol metabolism, choline metabolism in cancer, insulin resistance, sphingolipid signaling, taurine and hypotaurine metabolism, galactose metabolism, ABC transporters, primary bile acid biosynthesis, glycine, serine and threonine metabolism, glycerophospholipid metabolism, and arginine and proline metabolism. Moreover, the calculated differential abundance scores indicated the tendency of the active metabolites in each pathway to increase or decrease, compared with the controls [41] (Fig. 4C; 4D). Grouping of pathway hierarchies indicated that these differential pathways belonged to amino acid metabolism, cancer, carbohydrate metabolism, digestive system, endocrine and metabolic disease, lipid metabolism, membrane transport, metabolism of other amino acid, and signal transduction. All measured metabolites in ABC transporter, primary bile acid biosynthesis, cholesterol metabolism, and galactose metabolism pathways in the nAMD group were increased (calculated differential abundance scores = 1.0).

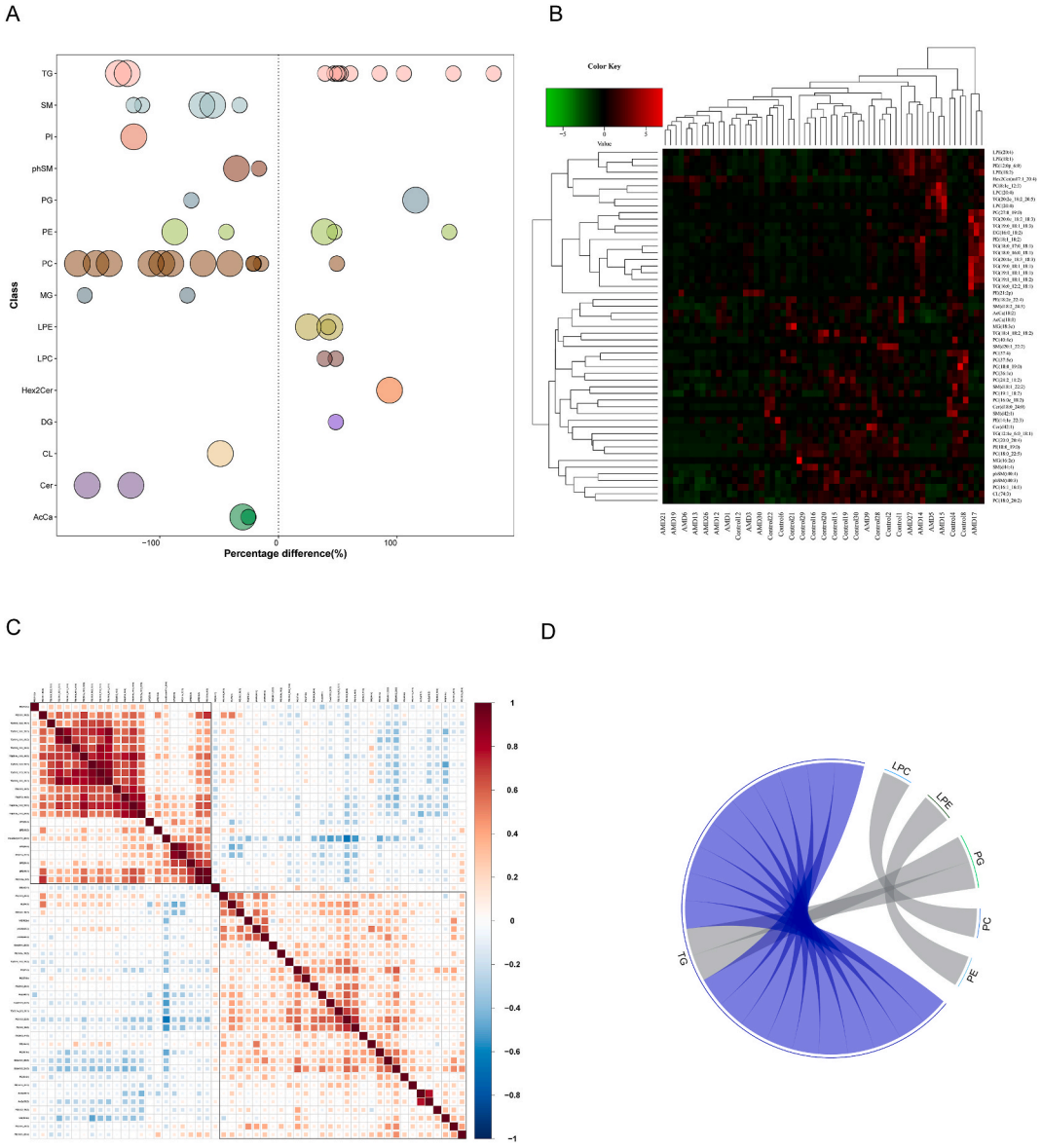

Fig. 5. Comparison of lipids differentially expressed between the nAMD and control groups. A: Relative percentage difference in concentration of all quantified lipid species. Each dot represents a lipid species, while dot size indicates significance. Different lipid classes are color-coded. B: Heat map providing a global overview of lipid abundance profiles in all evaluated plasma samples via hierarchical clustering analysis. C: Correlation matrix of lipids showing significant differences. Red and blue colors indicate positive and negative correlations, respectively, while whiter indicates non-significant correlations. Color intensity and circle size are proportional to the correlation coefficient (r). D: Network visualization of correlated lipid pairs ($r > 0.8$ by Pearson's correlation analysis). Each lipid is represented by a node around the circle plot and color coded according to its superclass. Lines connecting highly correlated pairs are color coded according to lipid class for intra-class correlation, and in dark-grey for inter-class correlation.

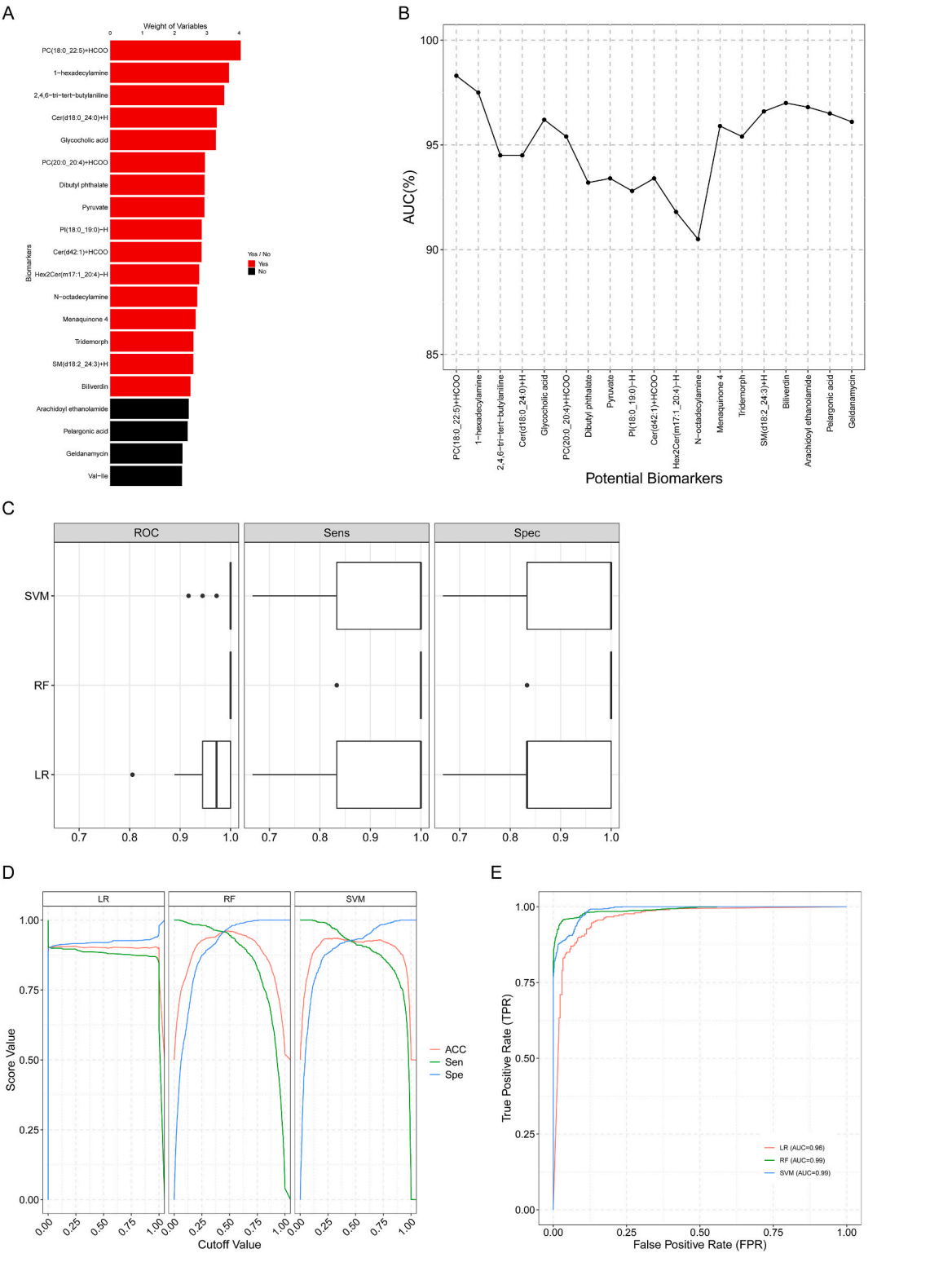

(caption on next page)

Fig. 6. Screening for potential nAMD biomarkers. A: Sample weight of potential biomarkers. B: cumulative area under the receiver operating characteristic (AUC) curves based on potential biomarkers. The top 16 metabolites and lipids in sample weight were: PC (18:0_22:5) + HCOO, 1-hexadecylamine, 2,4,6-tri-*tert*-butylaniline, Cer(d18:0_24:0) + H, glycocholic acid, PC(20:0_20:4) + HCOO, dibutyl phthalate, pyruvate, PI (18:0_19:0)-H, Cer(d42:1) + HCOO, Hex2Cer(m17:1_20:4)-H, Noctadecylamine, menaquinone4, tridemorph, SM(d18:2_24:3) + H, and biliverdin. C: Comparison of the performances of three machine learning methods in evaluating the diagnostic biomarker panel. D: Comparison of the accuracy, sensitivity, and specificity of three machine learning methods with the corresponding cutoff value in evaluating the diagnostic biomarker panel. LR: logistic regression; RF: random forest; SVM: support vector machine. E: Receiver operating characteristic (ROC) curves of the diagnostic panel model of biomarkers evaluated via three machine learning methods.

3.3. Lipidome profile of nAMD

The above-described Metabolomics data demonstrated that lipids and lipid-like molecules were the superclass that showed the highest numbers of significantly differentially expressed metabolites. Noteworthy, lipid composition varies under different conditions [42]. Hence, an untargeted lipidomics study was conducted next to identify and quantify lipid constituents in nAMD patients *vs.* controls. A total of 3082 individual lipid species belonging to 42 different lipid classes and six lipid categories (glycerophospholipids, sphingolipids, glycerolipids, sterol lipids, prenol lipids, and fatty acyls) were identified (Table S5). Of these, sphingolipids and glycerophospholipids were the top two type of lipid compounds with the highest number of identified lipid classes (17 and 15, respectively). Four glycerophospholipid classes (cardiolipin [CL], lysophosphatidylcholine [LPC], phosphatidylcholine [PC],

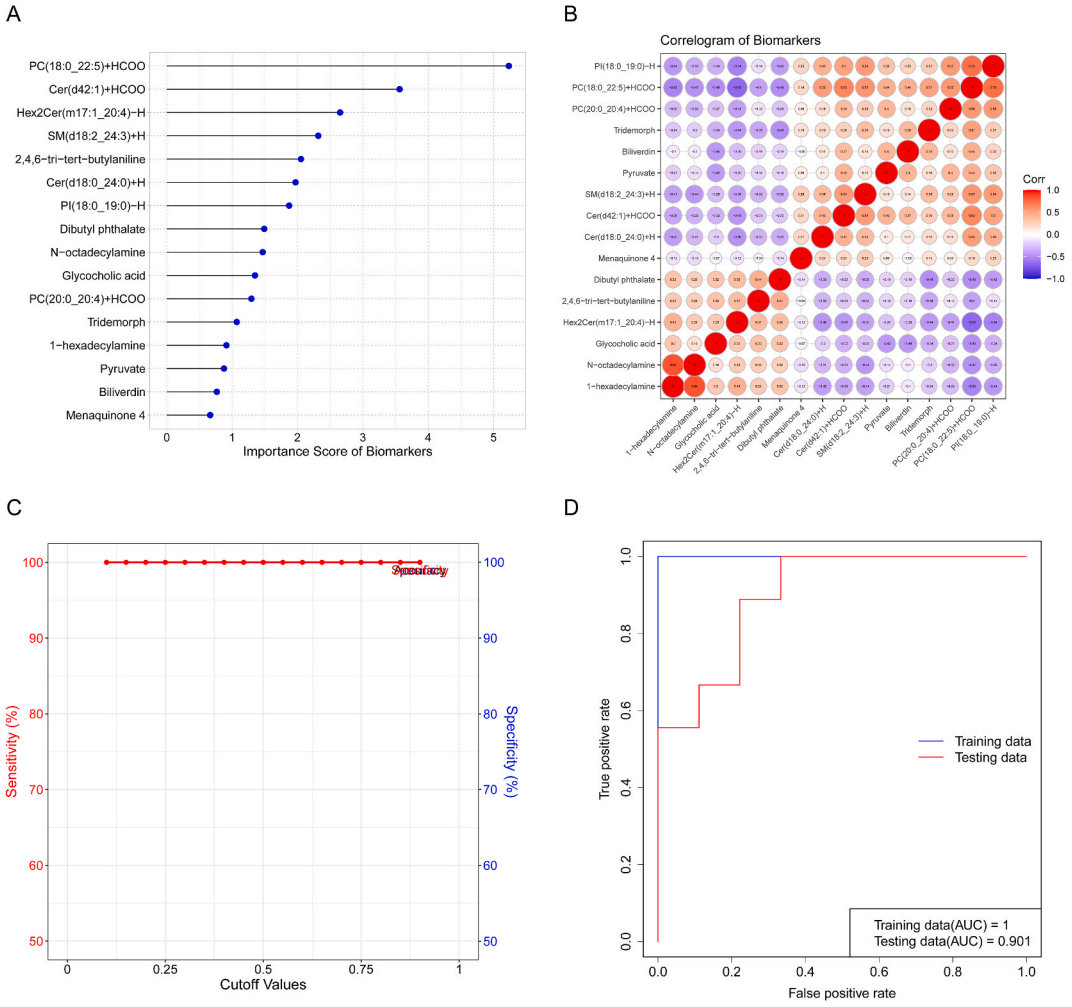

Fig. 7. Features of the biomarker panel. A: Importance score of biomarkers from the random forest model. B: Correlogram of biomarker panel values. Pearson's correlation coefficients (r) for all biomarkers are given in the circles. Colored circles indicate statistically significant correlations. Sizes and color intensities of the circles are related to the correlation coefficients. Red and blue colors represent positive and negative correlations, respectively. C: Cut-off value for accuracy, sensitivity and specificity was calculated using the Youden's index. D: ROC curves of the constructed diagnostic biomarker panel in the training and testing sets.

phosphatidylethanolamine [PE]), three sphingolipid classes (ceramide [Cer], hexosyl-ceramide [Hex2Cer], and sphingomyelin [SM]), and two glycerolipid classes (triglyceride [TG] and diglyceride [DG]) were the top nine lipid classes containing >100 identified lipid species.

Significant changes in the abundance of lipid species were observed among most lipid classes (Fig. 5A). Fifty-three lipids that were identified as being significantly different between the nAMD and control groups (Table S6) belonged to four major lipid categories and 15 lipid classes, as follows: glycerophospholipids (i.e., PC, PE, phosphatidylglycerol (PG), phosphatidylinositol (PI), LPC, lysophosphatidylethanolamine (LPE), and CL), sphingolipids (SM, Cer, Hex2Cer, and phytosphingosine (phSM)), glycerolipids (i.e., TG, DG, and monoglyceride (MG)), and fatty acyls (i.e., acyl carnitine (AcCa)). The contents of two glycerophospholipids (i.e., PE (21:2p) + H and PG (27:0_19:0) + H) and three glycerolipids (i.e., TG (20:0e_18:2_18:3) + Na, TG (20:1e_18:3_18:3) + H, TG (20:2e_18:2_20:5) + H) were increased by more than 3-fold than in the control samples. Among these, the TG (20:2e_18:2_20:5) + H showed the largest changes in terms of its amount.

As described in the aforementioned metabolite analysis, differentially expressed lipids with an OPLS-DA VIP score >1 and a $p < 0.05$ were used to conduct further applied bioinformatics analyses involving clustering, correlation, and pathway analyses that were then used to compare the lipidomic patterns between the nAMD and control groups. Differential lipids in all enrolled samples were visualized via a heatmap generated by hierarchical clustering which was based on the degree of similarity of lipid abundance profiles (Fig. 5B). Moreover, hierarchical clustering of the complete lipid-lipid correlation matrix revealed unique pairs of positively and negatively correlated lipids (Fig. 5C). A chord diagram that provides a further understanding of the possible regulatory relationship between lipid classes is presented in Fig. 5D. The lipid classes exhibited higher interclass correlations; interestingly, TGs showed both intra- and inter-class correlations.

3.4. Construction of the discriminative biomarker panel for nAMD

Noise signals and large amounts of detected metabolites restrict the accuracy and sensitivity of high-throughput "omics" analyses. In contrast to univariate statistical analysis, multivariate statistical machine learning methods can be used to construct predictive models that enable the detection of the most discriminative biomarker combinations [37]. The cumulative AUC curve generated by ROC analysis revealed that 16 metabolites and lipids were markedly different between the nAMD and control groups; namely, PC (18:0_22:5) + HCOO, 1-hexadecylamine, 2,4,6-tri-*tert*-butylaniline, Cer (d18:0_24:0) + H, glycocholic acid, PC(20:0_20:4) + HCOO, dibutyl phthalate, pyruvate, PI (18:0_19:0)-H, Cer (d42:1) + HCOO, Hex2Cer (m17:1_20:4)-H, N-octadecylamine, menaquinone 4, tridemorph, SM (d18:2_24:3) + H, and biliverdin (Fig. 6A and B). Among these discriminative biomarkers, eight belonged to three lipid categories: glycerophospholipids (*i.e.*, PC (18:0_22:5) + HCOO, PC (20:0_20:4) + HCOO, PI (18:0_19:0)-H); sphingolipids (*i.e.*, Cer (d18:0_24:0) + H, Cer (d42:1) + HCOO, Hex2Cer (m17:1_20:4)-H, SM (d18:2_24:3) + H); and prenol lipids (*i.e.*, menaquinone 4). To further validate the effect of these candidate biomarkers, three machine learning methods were used. A comparison of the performance of the LR, RF, and SVM methods in evaluating the diagnostic biomarker panel model is shown (Fig. 6C–E). The AUC values for the LR, RF, and SVM methods were 0.96, 0.99, and 0.99, respectively, indicating that the panel of discriminative biomarkers was able to effectively identify nAMD patients from controls. Based on the RF algorithm, an importance score was calculated for each biomarker in the panel (Fig. 7A), with higher importance scores indicating higher contribution to the classification effect between the groups [43]. The top three biomarkers with the highest importance scores were all lipids, one being glycerophospholipids (i.e., PC (18:0_22:5) + HCOO) and the other two being sphingolipids (i.e., Cer (d42:1) + HCOO and Hex2Cer (m17:1_20:4)-H). Importance scores of these top three biomarkers were 5.233645577; 3.562064195, and 2.651852678, respectively. To investigate the association between different biomarkers detected by our diagnostic panel, we generated a correlogram using Pearson's correlation coefficients (Fig. 7B). We then used the Youden index to define the best cutoff value for diagnostic decision making [36]. Noteworthily, when the cutoff was 0.5 (Fig. 7C), the optimal accuracy, specificity, and sensitivity were 100%, 100%, and 100%, respectively. To further assess the predictive performance of the herein predicted diagnostic biomarker panel, the dataset was divided again into training and testing sets in a 7:3 ratio, and ROC analysis was performed. The AUC values for the training and testing sets were 1 and 0.901, respectively, further demonstrating the good predictive performance of the diagnostic biomarker panel (Fig. 7D).

4. Discussion

In recent years, many efforts were made to improve our understanding on the association between metabolites and AMD; however, a global metabolic network that especially pertained to the lipidome profile in AMD was still warranted. Furthermore, whether metabolites or lipids could be used as discriminative AMD biomarkers, and consequently representing potential targets for the development of new therapeutic interventions, still needed to be clarified. Integrated omics approaches allow a much better understanding of the association between aberrant metabolomes and the pathogenesis of diseases [44]. Therefore, the construction of a global metabolic network which integrates metabolomics and lipidomics was still required to identify the metabolites underlying AMD development and progression [45].

Previously, metabolic studies on AMD were performed using various approaches based on metabolomics [46]. Using NMR or MS-based metabolomics, previous studies identified several differential metabolites in the plasma of nAMD patients compared with controls [9–11]. Moreover, studies using plasma or serum of patients with AMD reported discriminate metabolites that differed with disease stage [12–14,47]. Indeed, previous metabolic studies have indicated that dysregulated lipid metabolic pathways could play an important role in AMD development and progression [15].

Lipid metabolism is one of the main abnormal pathways in AMD [48]; however, to date, lipidomic studies in AMD are lacking. In

the present study, we used integrative metabolome and lipidome analyses and multivariate statistical machine learning methods to construct a discriminative biomarker panel, which comprised 16 metabolites and lipids, that collectively effectively distinguished nAMD patients from controls. Among these 16 discriminative biomarkers, eight were lipids that belonged to three lipid categories: glycerophospholipids; sphingolipids; and prenol lipids. Notably, the top three biomarkers with the highest importance scores were all lipids, including a glycerophospholipid (*i.e.*, PC (18:0_22:5) + HCOO) and two sphingolipids (i.e., Cer(d42:1) + HCOO and Hex2Cer (m17:1_20:4) - H). These results further proved the importance of lipid metabolic pathways, especially the glycerophospholipid and sphingolipid pathways, in nAMD. The findings of previous studies support the relevance of lipid-related metabolites, with particular reference to significant dysregulation of the glycerophospholipid pathway in AMD [14,49]. Glycerophospholipids, which constitute a major component of the lipid bilayer of cell membranes, are especially enriched in neural membranes, where they provide structural stability and fluidity [50]. Significant progress has been made in the understanding of the association between altered glycerophospholipids and neurodegenerative diseases, such as Alzheimer's and Parkinson's diseases [51,52]. Decreased levels of glycerophospholipids have also been suggested as a discriminative biomarker of AMD [14]. All glycerophospholipids in our discriminative biomarker panel were decreased in nAMD patients compared with controls, thus confirming the role of impaired cell membrane structure and function in AMD pathogenesis. In addition to glycerophospholipids, sphingolipids constitute another major component of membrane lipids [50]. Sphingolipids reportedly play a potential role in choroidal and retinal neovascularization, which are hallmarks of nAMD [53–55]. Similar to the alteration trends observed in glycerophospholipids, all SMs, a type of sphingolipid, in our discriminative biomarker panel were decreased in nAMD patients compared with controls. Accordingly, all Cers, which are hydrolyzed from SMs by sphingomyelinases, were also decreased in our discriminative biomarker panel.

In human lenses, Cer levels, which are barely detectable before the age of 30, increase with age [56,57]. However, nAMD patients and age-matched controls who were enrolled in this study were older than 50 years, thus making any comparison between age-related Cer levels unfeasible. Thus, the reduced Cer levels observed herein may be attributed to a type of late-stage AMD, namely nAMD. Using serum samples of two types of late-stage AMD, nAMD and GA, a previous study revealed that Cer species are increased in GA but not in nAMD, suggesting that specific lipid species may possibly play differential roles in the clinical variations observed in AMD [58]. Interestingly, the same study found increased serum levels of Hex-Cer in patients presenting both types of late-stage AMD [58], which agrees with the findings pertaining to nAMD of the current study, suggesting that sphingolipid levels in both non-neovascular and neovascular AMD subtypes may vary. Han et al. suggested that increased Cer mass levels may result from either accelerated SM hydrolysis or increased biosynthesis [59]. Given that the levels of glycerophospholipids and SMs (both of which are major components of membrane lipids) were found to be decreased in the current study, we hypothesize that reduced Cer levels are accompanied by reduced SMs "cargo," as reflected by the postulation that impaired cell membrane structure and function is associated with pathogenesis in AMD, as proposed by Laíns et al., [14]. In animal models, depletion of Cers caused by the inhibition of Cer synthases was shown to result in impaired vision, as evidenced by the significantly reduced amplitudes in scotopic a- and b-waves as well as oscillatory potentials recorded by electroretinogram [60]. Therefore, downregulation of Cers may exacerbate vision impairment in nAMD patients.

Our study had several limitations. Firstly, the sample size was relatively small. Secondly, previous studies demonstrated that early- and advanced-stage AMD share some (*e.g.*, glycerophospholipids pathway) plasma/serum metabolomic/lipidomic alterations [14,47]; however, it remains unclear why not all metabolomic/lipidomic alterations are shared between the different stages of AMD. In addition, given the nature of the untargeted metabolomics and lipidomics approaches used in this study, it was impossible to detect quantitative differences in lipid and metabolomic data. Furthermore, to be noted, in the high-throughput untargeted metabolomics, identification of the metabolites was performed by comparing the accuracy of the *m/z* value and MS/MS spectra with that contained in the database. Matching metabolite spectra against such huge in silico databases can give rise to false positive identifications, maximizing extracted aligned features while decreasing false positives is one of the main challenges in untargeted metabolomics [61,62]. Therefore; rigorous quality control measures should be employed and the results required careful interpretations. In this study, three detected metabolites, viz., tridemorph, sulfadoxin, and dibutyl phthalate were considered as suspicious false-positives, although these three metabolites have very high similarity/matching scores in the identification process (0.987, 0.998, 0.993, respectively). It is because of that the identification process in untargeted metabolomics is plagued by an inherent limitation: if signal peaks in the test results are closely resemble the theoretical spectrum within the database, they may erroneously be classified as corresponding to the theoretical compound, thus yielding false-positive outcomes. Overall, targeted metabolomic and lipidomic studies are warranted for further detection of quantitative differences in metabolites and lipids in nAMD. A comprehensive understanding of the metabolic/lipidic changes throughout AMD progression remain to be elucidated.

In conclusion, our findings provide evidences of a global metabolic network in nAMD patients. Differences between the metabolic and lipid profiles of nAMD patients and of elderly individuals without this condition provide a readout for the overall metabolic status of nAMD. Moreover, the discriminative biomarker panel herein described for nAMD may support the development of novel therapeutic interventions.

Ethics statement

The study was conducted according to the tenets of the Declaration of Helsinki and with the approval of the institutional review board from the Second Xiangya Hospital of Central South University (No. 2020-094).

Data availability

The data that support the findings of this study are available from the corresponding author upon reasonable request.

Author contribution statement

Tantai Zhao: Conceived and designed the experiments; Wrote the paper.
Jiani Li: Performed the experiments; Wrote the paper.
Yanbin Wang: Analyzed and interpreted the data.
Xiaojian Guo: Contributed reagents, materials, analysis tools or data.
Yun Sun: Conceived and designed the experiments; Analyzed and interpreted the data; Wrote the paper.

Declaration of competing interest

The authors declare that they have no known competing financial interests or personal relationships that could have appeared to influence the work reported in this paper.

Acknowledgments

This work is funded by the National Natural Science Foundation of China (Project No. 81900895), Natural Science Foundation of Hunan Province (Project No. 2020JJ5833 and 2020JJ4825), and Key Project of Research and Development Plan of Hunan Province (Project No. 2023SK2032).

Appendix A. Supplementary data

Supplementary data to this article can be found online at https://doi.org/10.1016/j.heliyon.2023.e20329.

References

[1] P.T. de Jong, Age-related macular degeneration, N. Engl. J. Med. 355 (14) (2006) 1474–1485.
[2] P. Mitchell, et al., Age-related macular degeneration, Lancet 392 (10153) (2018) 1147–1159.
[3] C.W. Wong, et al., Age-related macular degeneration and polypoidal choroidal vasculopathy in Asians, Prog. Retin. Eye Res. 53 (2016) 107–139.
[4] M. Fleckenstein, et al., Age-related macular degeneration, Nat. Rev. Dis. Prim. 7 (1) (2021) 31.
[5] R. Kawasaki, et al., The prevalence of age-related macular degeneration in Asians: a systematic review and meta-analysis, Ophthalmology 117 (5) (2010) 921–927.
[6] H. Hashemi, et al., Global and regional prevalence of age-related cataract: a comprehensive systematic review and meta-analysis, Eye (Lond) 34 (8) (2020) 1357–1370.
[7] M.W. Country, Retinal metabolism: a comparative look at energetics in the retina, Brain Res. 1672 (2017) 50–57.
[8] J. Wang, et al., Quantitative metabolomics of photoreceptor degeneration and the effects of stem cell-derived retinal pigment epithelium transplantation, Philos Trans A Math Phys Eng Sci (2016) 374, 2079.
[9] M.P. Osborn, et al., Metabolome-wide association study of neovascular age-related macular degeneration, PLoS One 8 (8) (2013), e72737.
[10] D. Luo, et al., Plasma metabolomic study in Chinese patients with wet age-related macular degeneration, BMC Ophthalmol. 17 (1) (2017) 165.
[11] J.M. Chao de la Barca, et al., A plasma metabolomic profiling of exudative age-related macular degeneration showing carnosine and mitochondrial deficiencies, J. Clin. Med. 9 (3) (2020).
[12] I. Lains, et al., Human plasma metabolomics in age-related macular degeneration (AMD) using nuclear magnetic resonance spectroscopy, PLoS One 12 (5) (2017), e0177749.
[13] I. Lains, et al., Human plasma metabolomics in age-related macular degeneration: meta-analysis of two cohorts, Metabolites 9 (7) (2019).
[14] I. Lains, et al., Human plasma metabolomics study across all stages of age-related macular degeneration identifies potential lipid biomarkers, Ophthalmology 125 (2) (2018) 245–254.
[15] X.W. Hou, Y. Wang, C.W. Pan, Metabolomics in age-related macular degeneration: a systematic review, Invest. Ophthalmol. Vis. Sci. 61 (14) (2020) 13.
[16] N.A. Iafe, N. Phasukkijwatana, D. Sarraf, Optical coherence tomography angiography of type 1 neovascularization in age-related macular degeneration, Dev. Ophthalmol. 56 (2016) 45–51.
[17] R.F. Spaide, et al., Consensus nomenclature for reporting neovascular age-related macular degeneration data: Consensus on neovascular age-related macular degeneration nomenclature study group, Ophthalmology 127 (5) (2020) 616–636.
[18] V. Matyash, et al., Lipid extraction by methyl-tert-butyl ether for high-throughput lipidomics, J. Lipid Res. 49 (5) (2008) 1137–1146.
[19] J. Xu, et al., Metabolomic analysis of aqueous humor identifies aberrant amino acid and fatty acid metabolism in vogt-koyanagi-harada and behcet's disease, Front. Immunol. 12 (2021), 587393.
[20] T. Liu, et al., Mass spectrometry-based metabolomics to reveal chicken meat improvements by medium-chain monoglycerides supplementation: taste, fresh meat quality, and composition, Food Chem. 365 (2021), 130303.
[21] Q. Chen, et al., Integrative analysis of metabolomics and proteomics reveals amino acid metabolism disorder in sepsis, J. Transl. Med. 20 (1) (2022) 123.
[22] S. Mi, et al., Characterization and discrimination of chilli peppers based on multi-element and non-targeted metabolomics analysis, Lebensmittel-Wissenschaft + Technologie 2020 (131) (2020), 109742.
[23] Y. Fu, et al., Degradation of lipid droplets by chimeric autophagy-tethering compounds, Cell Res. 31 (9) (2021) 965–979.
[24] Z. Hu, M. Zhang, Y. Tian, Screening and analysis of small molecular peptides in urine of gestational diabetes mellitus, Clin. Chim. Acta 502 (2020) 174–182.
[25] R. Adusumilli, P. Mallick, Data conversion with ProteoWizard msConvert, Methods Mol. Biol. 1550 (2017) 339–368.
[26] H. Ma, Y. Niu, Metabolomic profiling reveals new insight of fowl adenovirus serotype 4 infection, Front. Microbiol. 12 (2021), 784745.
[27] X.J. Zhang, et al., Pharmacological inhibition of arachidonate 12-lipoxygenase ameliorates myocardial ischemia-reperfusion injury in multiple species, Cell Metabol. 33 (10) (2021) 2059–2075 e10.

[28] R. Wang, et al., Gut microbiota regulates acute myeloid leukaemia via alteration of intestinal barrier function mediated by butyrate, Nat. Commun. 13 (1) (2022) 2522.
[29] M. Shang, et al., The folate cycle enzyme MTHFD2 induces cancer immune evasion through PD-L1 up-regulation, Nat. Commun. 12 (1) (2021) 1940.
[30] J. Xiang, et al., Gluconeogenic enzyme PCK1 deficiency promotes CHK2 O-GlcNAcylation and hepatocellular carcinoma growth upon glucose deprivation, J. Clin. Invest. 131 (8) (2021).
[31] L. Zhao, et al., Saturated long-chain fatty acid-producing bacteria contribute to enhanced colonic motility in rats, Microbiome 6 (1) (2018) 107.
[32] Y. Djoumbou Feunang, et al., ClassyFire: automated chemical classification with a comprehensive, computable taxonomy, J. Cheminf. 8 (2016) 61.
[33] R. Blanco-Dominguez, et al., A novel circulating MicroRNA for the detection of acute myocarditis, N. Engl. J. Med. 384 (21) (2021) 2014–2027.
[34] L.T. Hoang, et al., Transcriptomic signatures for diagnosing tuberculosis in clinical practice: a prospective, multicentre cohort study, Lancet Infect. Dis. 21 (3) (2021) 366–375.
[35] M. Greiner, D. Pfeiffer, R.D. Smith, Principles and practical application of the receiver-operating characteristic analysis for diagnostic tests, Prev. Vet. Med. 45 (1–2) (2000) 23–41.
[36] E.F. Schisterman, et al., Optimal cut-point and its corresponding Youden Index to discriminate individuals using pooled blood samples, Epidemiology 16 (1) (2005) 73–81.
[37] G. Peddinti, et al., Early metabolic markers identify potential targets for the prevention of type 2 diabetes, Diabetologia 60 (9) (2017) 1740–1750.
[38] Y. Gao, et al., Tetrahydroxy stilbene glycoside attenuates acetaminophen-induced hepatotoxicity by UHPLC-Q-TOF/MS-based metabolomics and multivariate data analysis, J. Cell. Physiol. 236 (5) (2021) 3832–3862.
[39] N. Goffard, T. Frickey, G. Weiller, PathExpress update: the enzyme neighbourhood method of associating gene-expression data with metabolic pathways, Nucleic Acids Res. 37 (2009) W335–W339 (Web Server issue).
[40] M. Schmidt, et al., Multi-scale account of the network structure of macaque visual cortex, Brain Struct. Funct. 223 (3) (2018) 1409–1435.
[41] A.A. Hakimi, et al., An integrated metabolic atlas of clear cell renal cell carcinoma, Cancer Cell 29 (1) (2016) 104–116.
[42] R. Aviram, et al., Lipidomics analyses reveal temporal and spatial lipid organization and uncover daily oscillations in intracellular organelles, Mol. Cell 62 (4) (2016) 636–648.
[43] V.A. Huynh-Thu, et al., Statistical interpretation of machine learning-based feature importance scores for biomarker discovery, Bioinformatics 28 (13) (2012) 1766–1774.
[44] X. Wan, et al., Metabolic profiling of amino acids associated with mortality in patients with acute paraquat poisoning, Med Sci Monit 24 (2018) 1397–1407.
[45] E.M. van Leeuwen, et al., A new perspective on lipid research in age-related macular degeneration, Prog. Retin. Eye Res. 67 (2018) 56–86.
[46] C.N. Brown, et al., Metabolomics and age-related macular degeneration, Metabolites 9 (1) (2018).
[47] E. Kersten, et al., Metabolomics in serum of patients with non-advanced age-related macular degeneration reveals aberrations in the glutamine pathway, PLoS One 14 (6) (2019), e0218457.
[48] M.A. Brantley Jr., et al., Plasma biomarkers of oxidative stress and genetic variants in age-related macular degeneration, Am. J. Ophthalmol. 153 (3) (2012) 460–467 e1.
[49] G. Chen, et al., Customized Consensus spectral library building for untargeted quantitative metabolomics analysis with data independent acquisition mass spectrometry and MetaboDIA workflow, Anal. Chem. 89 (9) (2017) 4897–4906.
[50] T. Harayama, H. Riezman, Understanding the diversity of membrane lipid composition, Nat. Rev. Mol. Cell Biol. 19 (5) (2018) 281–296.
[51] M. Kosicek, S. Hecimovic, Phospholipids and Alzheimer's disease: alterations, mechanisms and potential biomarkers, Int. J. Mol. Sci. 14 (1) (2013) 1310–1322.
[52] H. Xicoy, B. Wieringa, G.J.M. Martens, The role of lipids in Parkinson's disease, Cells 8 (1) (2019).
[53] B. Xie, et al., Blockade of sphingosine-1-phosphate reduces macrophage influx and retinal and choroidal neovascularization, J. Cell. Physiol. 218 (1) (2009) 192–198.
[54] S. Caballero, et al., Anti-sphingosine-1-phosphate monoclonal antibodies inhibit angiogenesis and sub-retinal fibrosis in a murine model of laser-induced choroidal neovascularization, Exp. Eye Res. 88 (3) (2009) 367–377.
[55] R. Terao, H. Kaneko, Lipid signaling in ocular neovascularization, Int. J. Mol. Sci. 21 (13) (2020).
[56] J.R. Hughes, et al., Instability of the cellular lipidome with age, Age (Dordr) 34 (4) (2012) 935–947.
[57] M. Trayssac, Y.A. Hannun, L.M. Obeid, Role of sphingolipids in senescence: implication in aging and age-related diseases, J. Clin. Invest. 128 (7) (2018) 2702–2712.
[58] L.M. Pujol-Lereis, et al., Evaluation of serum sphingolipids and the influence of genetic risk factors in age-related macular degeneration, PLoS One 13 (8) (2018), e0200739.
[59] X. Han, et al., Metabolomics in early Alzheimer's disease: identification of altered plasma sphingolipidome using shotgun lipidomics, PLoS One 6 (7) (2011), e21643.
[60] B. Bruggen, et al., Defective ceramide synthases in mice cause reduced amplitudes in electroretinograms and altered sphingolipid composition in retina and cornea, Eur. J. Neurosci. 44 (1) (2016) 1700–1713.
[61] C.H. Johnson, et al., Bioinformatics: the next frontier of metabolomics, Anal. Chem. 87 (1) (2015) 147–156.
[62] I.T. Ismail, M.R. Showalter, O. Fiehn, Inborn errors of metabolism in the era of untargeted metabolomics and lipidomics, Metabolites 9 (10) (2019).